HyPer-QuarCh II: a laboratory-scale device for hydrogen isotopes permeation experiments

HyPer-QuarCh II: a Laboratory-scale Device for Hydrogen Isotopes Permeation Experiments

L. Candido[a,*], C. Alberghi[a], A. Antonelli[b], S. Bassini[b], M. Piccioni[c], S. Storai[b], R. Testoni[a], M. Utili[b], M. Zucchetti[a,d]

[a] *ESSENTIAL Group, Politecnico di Torino - Corso Duca degli Abruzzi, 24, 10129, Torino, Italy*
[b] *ENEA C.R. Brasimone – Località Brasimone, 40043 Camugnano (BO), Italy*
[c] *Università di Bologna - Viale del Risorgimento, 2, 40136 Bologna (BO), Italy*
[d] *MIT, Massachusetts Institute of Technology, Cambridge (MA), US*

Abstract

In a D-T fusion reactor, the correct estimation of the tritium inventory and permeation fluxes towards the coolant and to the external environment is a crucial issue for the reactor licensing. Within this frame, a fast and reliable sensor for the online measurement of hydrogen isotopes concentration in the breeder is therefore necessary. At ENEA Brasimone research centre, Italy, the development, qualification and characterization of hydrogen isotopes permeation sensors (HPS) were carried out since the early 2000s. A new experimental laboratory-scale device, named Hyper-Quarch II (Hydrogen Permeation Quartz Chamber), was developed on the basis of the experience gained in the past experimental campaigns. This device is characterised by an upgraded test section in quartz and new instrumentation equipment, and will be used to test advanced hydrogen permeation sensor in both gas phase and in stagnant LiPb eutectic alloy (15.7 at.% Li). Hydrogen or deuterium will be adopted instead of tritium to simulate the operative conditions of the Water-Cooled Lithium-Lead (WCLL) Test Blanket Module of ITER and the WCLL Breeding Blanket of the European DEMO reactor. Moreover, the upgrade was performed to also allow the measurement of the Sieverts' constant of hydrogen or deuterium solubilised in the LiPb with absorption or desorption techniques in a temperature range from 300 to 550 °C and pressure range 0.1 to 100 hPa.

Keywords: HyPer-QuarCh II, Hydrogen Isotopes, Permeation, Sieverts' constant, ITER, DEMO

1. Introduction

In the Water-Cooled Lithium-Lead (WCLL) Test Blanket Module (TBM) of ITER [1] and in the WCLL breeding blanket of the European DEMO reactor [2], one of the most compelling issues is tritium management and, in particular, an accurate and reliable estimate of the tritium inventory in the liquid lithium-lead breeder (LiPb, 15.7 at.% Li) and in the structural materials, and the prediction of tritium permeation into the coolant and the external environment [3, 4]. Concerning the measurement of hydrogen isotopologues (Q=H,D,T), several technologies can be adopted, for which an extensive review can be found in [5]. In the last two decades, ENEA C. R. Brasimone, in collaboration with Politecnico di Torino, has developed hydrogen isotope permeation sensors (HPS) [6, 7, 8] for near real-time in-process tritium measurement in both liquid metals and gas phases. Moreover, due to the low solubility of hydrogen isotopes in LiPb, an important research topic regards some key properties of the liquid metal, such as the Sieverts' constant, which, despite several experiments carried out in the past, is characterised by significant discrepancies of up to several orders of magnitude [9], depending on the different methodologies adopted for its determination. With the absorption technique, the measure of Sieverts' constant is more than two orders of magnitude higher than with the desorption technique. This remarkable discrepancy may be due to some inaccuracies during the tests, as discussed in Chapter 4. One of the main objectives of HyPer-QuarCh II is to measure the same value with both absorption and desorption techniques.

In order to meet the need for a laboratory-scale device for the qualification and characterisation of HPS in stagnant lithium-lead and to measure the Sieverts' constant with both measurement techniques, an upgrade of the HyPer-QuarCh (Hydrogen Permeation Quartz Chamber) experimental device was performed. More specifically, compared to the previous version [10, 11], HyPer-QuarCh II has been designed to allow tests at both ITER and DEMO partial pressure conditions (1-10 Pa and 100-1000 Pa in LiPb, respectively) in a temperature range from 300 °C to 550 °C, and to measure the Sieverts' constant in absorption and desorption modes, also using HPS. The upgraded facility includes a quartz chamber with glass-to-metal connections, an internal quartz filling volume, a tungsten crucible, an external infrared heating system and special connections that can operate at high temperatures.

*Corresponding author
Email address: luigi.candido@polito.it (L. Candido)

The work is organised as follows. Chapter 2 presents the design of the new system. Chapter 3 describes the operation of the hydrogen permeation sensor, while Chapter 4 is devoted to describing the techniques used to measure the Sieverts' constant. Finally, Chapter 5 presents the numerical calculations performed to support the design, with emphasis on the thermal and transport analyses.

2. Design of HyPer-QuarCh II

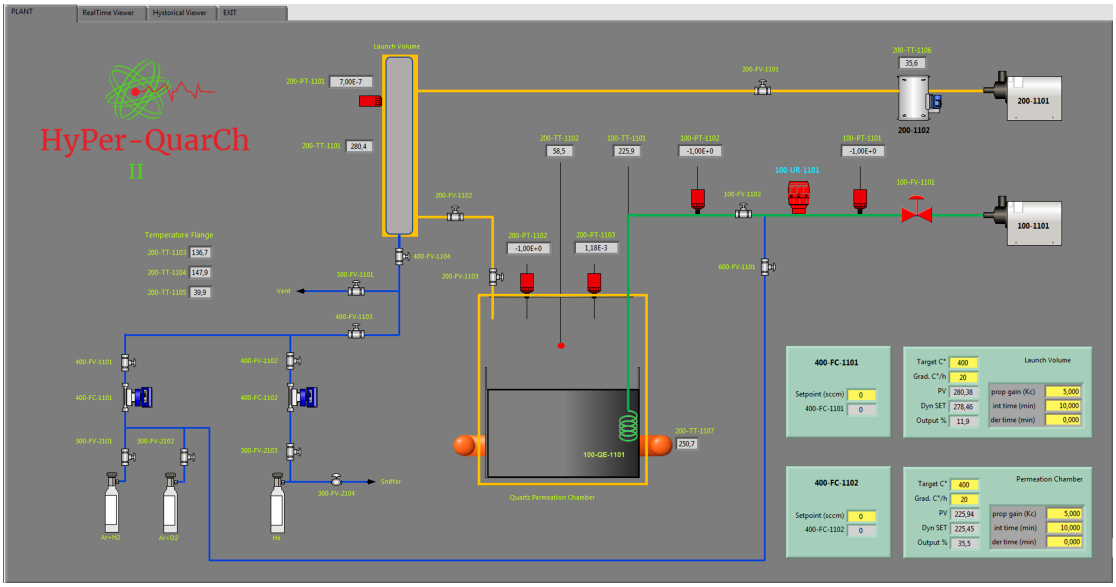

Figure 1: Synoptic of HyPer-QuarCh II experimental device. In green: sensor line, subsystem 100; in orange: launch volume and test section line, subsystem 200; in blue: gas lines, subsystems 300-600.

This chapter aims to present the upgrade of HyPer-QuarCh (Hydrogen Permeation Quartz Chamber) [12], with the aim of qualifying hydrogen isotopes permeation sensors in both gas phase and liquid phase. Moreover, the upgrade of the facility regards the possibility to measure the Sieverts' constant of hydrogen or deuterium solubilized in the liquid lithium-lead eutectic alloy. The synoptic of the device is displayed in Figure 1. The nomenclature was chosen according to ISA 5.1-1982 (R1992). The device is constituted by 6 different subsystems hereafter reported:

- Sensor line (100);
- Launch volume and test section (200);
- Gas lines (storage line 300, service line 400, discharge line 500, calibration line 600).

In the following sections, the description of the above-mentioned classification of the subsystems as well as the installed instruments.

2.1. Sensor line

The sensor line is constituted by the 100-QE-1101 helical-shaped hydrogen isotopes permeation sensor (HPS) realised in 99.5% pure α-iron (bcc), and all the connections and instrumentation up to its vacuum pumping system. The sensor was welded to a 1/8" pipe through a GTAW technique and leak tested.

Figure 2: Sensor line, subsystem 100. 1: Diaphragm/turbomolecular pumping station. 2: Electro-pneumatic valve. 3: Capacitive pressure transducer. 4: Quadrupole mass spectrometer. 5: Gate valve. 6: Capacitive pressure transducer. 7: z-axis manipulator. 8: Hydrogen isotopes permeation sensor.

Table 1: Components and instrumentation for Subsystem 100 - Sensor line.

Identification	Type	Operative pressure [hPa]
100-1101	Pumping station	$\leq 10^{-7}$ (ultimate pressure)
100-FV-1101	Electropneumatic valve	$10^{-8} - 2000$
100-PT-1101	Capacitive pressure transducer	$10^{-5} - 0.11$
100-UR-1101	Faraday/SEM mass spectrometer	$\leq 10^{-5}$
100-FV-1102	Gate valve	$10^{-7} - 1000$
100-PT-1102	Capacitive pressure transducer	0.01 -110
100-TT-1101	Thermocouple type K	-
100-QE-1101	Q_2 permeation sensor	0.1-100

The sensor was then connected through a 1/4" pipe to a z-axis manipulator with 50 mm stroke to allow the movement into and out of the LiPb; a thermocouple (100-TT-1101) is used to monitor the temperature of the sensor walls and of LiPb when the sensor is submerged. A high-precision ($\pm 0.15\%$ on the measured value) capacitive pressure transducer (100-PT-1102) is installed before the interception gate valve 100-FV-1102 and it is able to read the pressure due to the hydrogen isotopes permeation in the range 0.01-110 hPa. The rest of the line accounts for a quadrupole mass spectrometer (100-UR-1101) able to read the gas concentration in the range 1-50 amu by using a Faraday/C-SEM detector and a capacitive transducer 100-PT-1101 operating between $1 \cdot 10^{-5} - 110$ hPa. The sensor line is kept below 10^{-5} hPa in order to correctly operate the mass spectrometer. The quadrupole mass spectrometer and the pressure transducer can be intercepted by means of an electro-pneumatic valve (100-FV-1101) from the pumping station 100-1101, constituted by a diaphragm pump and a turbomolecular pump embedded into an integrated pumping station. A list of the components is detailed in Table 1. The 3D CAD view of the sensor line is given in Figure 2.

2.2. Launch volume and test section

The launch volume was conceived to heat the mixture argon/hydrogen or deuterium up to 550 °C prior to its injection into the test section. It is constituted by a 505 mm (height) x 84 mm (external diameter) cylindrical vessel realised in AISI 316 stainless steel; it interfaces with the gas service line 400 for the preheating of the gas mixture and has three more penetrations to host the instrumentation and the connection to the vacuum pumping system and to the permeation chamber. The instrumentation is installed through a DN 40 CF cross which hosts the internal thermocouple for the gas temperature measurement, a full range pressure transducer (200-PT-1101) and the connection to the helium leak detector to allow leakage tests.

The pumping system is constituted by a roots pump (200-1101) which realises a rough vacuum for the turbomolecular pump. This pumping system can be intercepted by means of the 200-FV-1101 bellows sealed valve. The roots pump was chosen due to its dry rotating parts, preventing any possible oil contamination in the facility. Two valves, labelled 200-FV-1102 and 200-FV-1103, are installed upstream and downstream of the flexible corrugated hose connecting the launch volume and the quartz chamber in order to intercept the launch volume and the test section, respectively.

Figure 3: Launch volume/test section, subsystem 200. 1: Roots pump. 2: Turbomolecular pump. 3: Bellows sealed valve. 4: Full range pressure transducer. 5: Launch volume. 6: Bellows sealed valve. 7: Gate valve. 8-9: Capacitive pressure transducers. 10: Test section.

The test section (TS, Figure 4) is realised in quartz glass because of the low permeability to hydrogen isotopes. The quartz chamber is 26.5 cm high, has an outer diameter of 15.5 cm and a wall thickness of 1.5 cm. In the upper part of the chamber, a connecting flange of 20 cm OD is coupled to an upper flange hosting three sleeves with quartz-to-metal connections. The sleeves have external grooves in which O-rings are housed to ensure the connection between the stainless steel KF connections and the sleeves. The seal between the flange and the chamber is ensured by a nitrile rubber O-ring resistant up to 150 °C.

Table 2: Components and instrumentation for Subsystem 200 - Launch volume/test section.

Identification	Type	Operative pressure [hPa]
200-1101	Roots pump	$\leq 10^{-2}$ (ultimate pressure)
200-1102	Turbomolecular pump	$\leq 10^{-9}$ (ultimate pressure)
200-FV-1101	Bellows sealed valve	-
200-PT-1101	Full range pressure transducer	$5 \cdot 10^{-9} - 1000$
200-FV-1102	Bellows sealed valve	Up to 10^{-9}
200-FV-1103	Gate valve	Up to 10^{-7}
200-PT-1102	Capacitive pressure transducer	$0.01 - 100$
200-PT-1103	Capacitive pressure transducer	$10^{-4} - 1.1$
200-TT-1101/07	Thermocouple type K	-

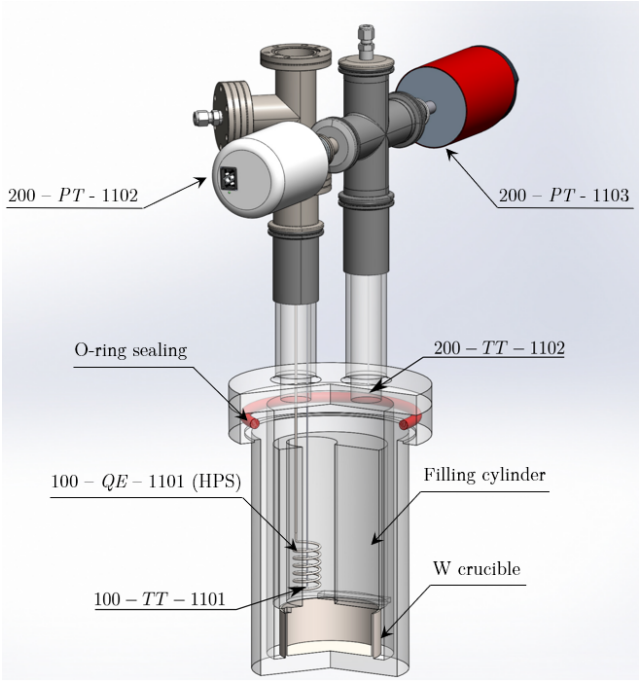

Figure 4: 3D drawing of the test section.

One of the sleeves is connected to a DN 40 CF cross hosting the instrumentation for the chamber, constituted by two capacitive pressure transducers (200-PT-1102 and 200-PT-1103) and a thermocouple to monitor the temperature in the upper part of the chamber and in proximity of the sealing. Inside the permeation chamber, a tungsten crucible containing the LiPb is positioned. The launch volume/test section CAD drawing is displayed in Figure 3.

To reduce the internal volume of the chamber, a 16 cm x 11.3 cm (height x diameter) quartz filling cylinder, equipped with a through hole to allow the passage of the sensor, is placed above the crucible and spaced from it by two 0.5 cm high quartz strips. In this way, the internal volume was reduced by 44% with the adoption of the filling cylinder. The tungsten crucible is heated by a 500 W infrared collar made of quartz with a gold shielding to collimate the electromagnetic radiation. The collar is located outside the quartz chamber, which is almost transparent to electromagnetic radiation, so that reasonable temperatures can be reached in the upper part, as shown in Chapter 5.

The procedure for the filling of LiPb into the W crucible was carried out in a dedicated stainless steel capsule to minimize the content of impurities in the melt. The capsule has penetrations in the cover flange to allow the arrangement of the vacuum and inert gas supply lines and the introduction of K-type thermocouples into the LiPb melt. The W crucible (4.5 cm height x 10 cm diameter) is placed in the bottom of the steel capsule during melting. Pieces of LiPb eutectic alloy were cut from an ingot in the right amount to obtain the desired volume in the tungsten crucible (239 cm^3). To minimize oxygen contamination, the LiPb pieces were first ground with abrasive papers to obtain a bright surface without the typical ingot crust. The ground LiPb pieces were then immediately placed in the W crucible and sealed in the steel capsule under argon overpressure (99.9999% vol. purity, 0.2-0.3 barg).

To reduce atmospheric contaminants (moisture, oxygen, CO_2) during the melting procedure in the capsule, four alternating vacuum cycles are performed with argon gas injection. Then, vacuum is generated at 130 °C and then at 180 °C respectively for 1 day. Finally, the LiPb was resealed under argon overpressure (0.2-0.3 barg) and the temperature was heated to about 300 °C to allow complete melting. Cooling of the LiPb was then performed under argon overpressure. The main components and instrumentation are given in Table 2. A detail of the top quartz flange is shown in Figure 5.

2.3. Gas lines

The gas lines 300, 400, 600 are devoted to the supply of the Ar-H_2 mixture (calibrated tank, 2.99% H_2), the D_2 gas and the He gas to the system. Two mass flow controllers 400-FIC-1101 and 400-FIC-1102 are used to inject Ar-H_2 or D_2 and He to the system, respectively. The injection of gas into the launch volume is also controlled through a millimetric gas dosing valve in order to have a double control on the gas admitted.

Figure 5: Upper flange with quartz-to-metal connections.

The line 500 is used to discharge the gas into the atmosphere by means of the ball valve 500-FV-1101. The different type of gas to be injected into the launch volume and then into the quartz chamber can be selected by opening or closing the 400-FV-1101 and 400-FV-1102 bellows sealed valves. A by-pass before the 400-FIC-1101 mass flow controller was installed in order to provide the Ar-H_2 mixture to the mass spectrometer with the purpose of calibration. The calibration line, 600, is equipped with a diaphragm valve which separates it from the sensor line.

2.4. Final assembly

In Figure 6, the full assembly of HyPer-QuarCh II is displayed. The main operative parameters of the device are reported in Table 3. It has to be observed that the maximum temperature achievable (450 °C) is limited by the maximum allowable temperature for the gasket sealing of the CF connections present in the launch volume.

Table 3: Main design parameters of HyPer-QuarCh II.

Parameters	Value	Units
Q_2 partial pressure	0.1-100	hPa
Operative temperature	300-550	°C
Q_2 concentration (calibrated tank)	2.99	Vol. %
Max. temperature	650	°C
Max. operative pressure in the TS	1200	hPa
Vol. of TS (with filling cylinder)	1694	cm^3
Vol. of TS (without filling cylinder)	3040	cm^3

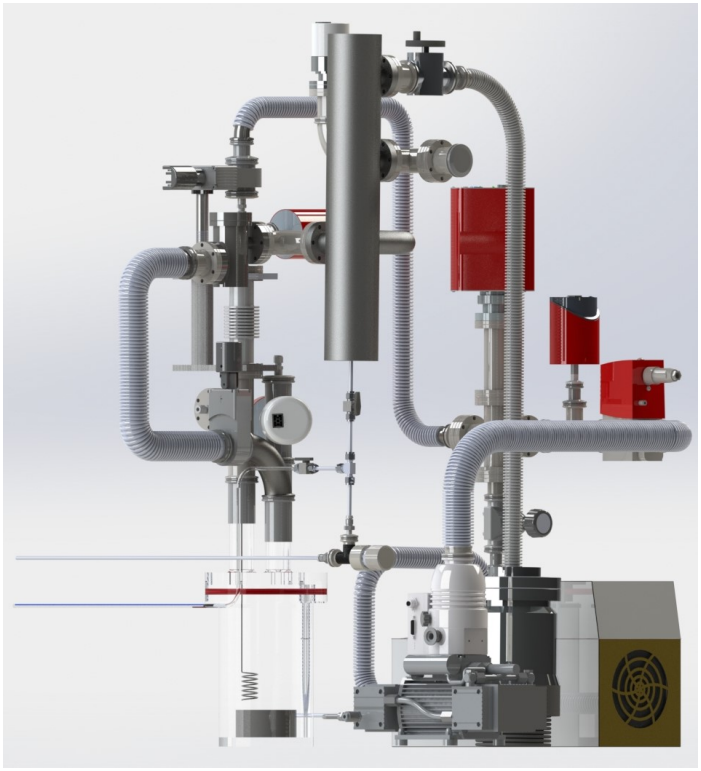

Figure 6: Full assembly of HyPer-QuarCh II.

3. Operational modes of the hydrogen permeation sensor

HyPer-QuarCh II is designed for the characterization of hydrogen isotopes permeation sensors (HPS) and for the determination of the Sieverts' constant of hydrogen or deuterium in static LiPb. In this setup, the design chosen for the HPS was derived from a previous study [8] and optimized according to the fabrication requirements, Figure 7. The characteristics of the actual permeation sensor installed are given in Table 4. The use of a HPS during the measurement of the Sieverts' constant allows a) monitoring of the pressure inside the LiPb during testing (hydrogen is dissolved in LiPb in monatomic form) and b) a double check between the partial pressure in the cover gas (where hydrogen is in molecular form) and in the LiPb. Other technologies, such as electrochemical sensors, are promising, but there are few applications, especially for Gen-IV fast reactors, and at the current state of the art their accuracy depends on calibration in the reactor environment, especially the operating temperature of the reactor [13], which limits the temperature range of applicability. Under the EUROfusion program, specific R&D activities related to the development of electrochemical sensors and to better define some performace indicators (such as accuracy, precision, linearity, etc.) for the HPS are planned in the period 2021-2025.

The helical design allows to reduce the number of weldings, therefore minimising the problem of iron oxidation during the welding procedure and reducing the costs. Only

two welds are needed: a butt weld at the bottom of the pipe, in order to close it, and an orbital weld at the top, so as to directly connect the helix with a 1/8" Swagelok pipe. To facilitate the connection to the rest of the system 100 and to increase the conductance of the line without increasing significantly the internal volume, the 1/8" pipe is connected through an adapter to a 1/4" pipe. The sensor can work in two operational modes: the *equilibrium mode* and the *dynamic mode*.

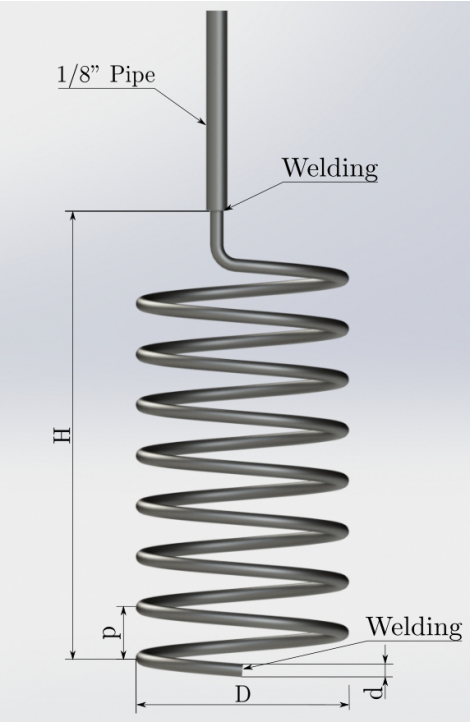

Figure 7: Hydrogen permeation sensor installed in HyPer-QuarCh II device.

Table 4: Geometrical characteristic of optimised HPS.

Parameter	Value	Units
Minor diameter, d	2.0	mm
Major diameter, D	26	mm
Pitch between coils, p	7.6	mm
Height of the sensor, H	60	mm
Thickness, t_s	0.20	mm
Angle between coils, α	5.7	°
Number of coils, N	8	-
Total tube length, l_{tot}	600	mm

3.1. Equilibrium mode

In equilibrium mode, starting from vacuum conditions, there is an increase in pressure inside the membrane of the sensor due to the flow of hydrogen isotopes permeated through its walls. In this operational mode, the line is intercepted by the gate valve 100-FV-1102. The pressure inside the measuring head changes until its value is equal to the partial pressure of hydrogen solubilized in the lithium-lead. Once this value is measured by the pressure transducer 100-PT-1102, it is possible to derive the concentration of hydrogen isotopes solubilized in the liquid phase through the Sieverts' law:

$$c_{Q,l} = k_{s,l} \cdot \sqrt{p_{eq,Q_2}} \tag{1}$$

where $c_{Q,l}$ [mol m^{-3}] is the hydrogen isotopes concentration in LiPb, $k_{s,l}$ [mol m^{-3} Pa$^{-1/2}$] is the Sieverts' constant of Q species in liquid LiPb and p_{eq,Q_2} [Pa] is the equilibrium partial pressure of gaseous hydrogen isotopes above the free surface of the lithium-lead. Sieverts' law assumes that the partial pressure of hydrogen in gas phase (p_{Q_2}) and the partial pressure of hydrogen solubilized in liquid phase (p_Q) reach an equilibrium condition, for which it results that $p_{Q_2} = p_Q$; it has to be observed that the hydrogen isotope is dissolved in its monoatomic form in the liquid metal, whereas in gas phase it is found in diatomic form. The results provided in the equilibrium mode operation are influenced mainly by the accuracy on Sieverts' constant. Only the pressurization time of the capsule is influenced by the rate of permeation (which is a characteristic of the membrane properties), not the final pressure, which is the only measurement required. A first estimation of the accuracy based on qualification in gas phase on TRIEX-II facility at ENEA C.R. Brasimone showed it varies from 3 to 7% [14]. It has to be observed that the gradient of pressure between the high pressure side of the membrane and the lower pressure side decreases with time [12]; this implies that the time to reach the asymptotic condition of the pressure rise is much higher than that in the case of a constant pressure gradient, which is the characteristic of the dynamic mode, where vacuum is continuously pumped inside the membrane. An extensive description of the mathematical formulation of the operation in equilibrium mode in both gas and liquid phases can be found in [15] and [14].

3.2. Dynamic mode

In dynamic mode, a measurement of the permeation flux, J [mol m^{-2} s^{-1}], is assessed by means of the quadrupole mass spectrometer. The gate valve 100-FV-1102 is open and vacuum is continuously pumped by the 100-1101 pumping station. In this operational mode, the permeation flux depends on the membrane characteristics, i.e. diffusivity, Sieverts' constant and surface parameters of the material [16], according to the permeation regime. More details on the different permeation regimes in presence of liquid metals and a membrane can be found in [17].

4. Sieverts' constant measurement with absorption and desorption techniques

In the absorption tests, after the system is evacuated, the hydrogen (we refer to hydrogen here, but the reasoning

is the same as for deuterium) is injected until the required pressure p_0 is reached. Then, at $t = t_0$, the chamber is isolated and the hydrogen begins to be solubilized in the LiPb until equilibrium between the pressures, called p_{end}, of the gas phase and the liquid phase is reached, at $t = t_{end}$. This pressure is the same that the HPS would measure: in fact, the hydrogen partial pressure in the LiPb at equilibrium is the same as in the cover gas, according to Sieverts' law; in this way, it is possible to perform a double check of the pressure, since the first one is given by the pressure measurement in the cover gas of the test section. Sieverts' constant can be determined from the absorption tests by establishing a molar balance between the times $t = t_0$ and $t = t_{end}$. If there are negligible absorptions/losses of hydrogen in the system, the molar balance must be guaranteed between $t = t_0$ and $t = t_{end}$, which gives:

$$n_{gas,0} + n_{LiPb,0} = n_{gas,end} + n_{LiPb,end} \quad (2)$$

where $n_{gas,0}$ and $n_{LiPb,0}$ are the number of hydrogen moles in the cover gas and the LiPb at $t = t_0$, whereas $n_{gas,end}$ and $n_{LiPb,end}$ are the same quantities but evaluated at $t = t_{end}$. It is easy to demonstrate that the different contributions to the molar balance can be expressed as follow, assuming an ideal behaviour of the gas:

$$2\frac{p_0 V_{gas}}{RT_{gas}} + 0 = 2\frac{p_{end} V_{gas}}{RT_{gas}} + k_{S,abs}\sqrt{p_{end}} V_{LiPb} \quad (3)$$

Here, V_{gas} and T_{gas} are the gas volume and temperature, V_{LiPb} is the volume of the lithium-lead and R is the universal gas constant. Therefore, the Sieverts' constant can be calculated from Equation 3, which gives, for absorption tests:

$$k_{S,abs} = \frac{2}{RT_{gas}} \frac{V_{gas}}{V_{LiPb}} \frac{p_0 - p_{end}}{\sqrt{p_{end}}} \quad (4)$$

On the other hand, the desorption tests start from the equilibrium condition of the hydrogen partial pressure, p_0, between the LiPb and cover gas, followed by a rapid pumping down of the cover gas. In this case, the different terms in the mass balance equation, Equation 2, read:

$$0 + k_{S,des}\sqrt{p_0} = 2\frac{p_{end} V_{gas}}{RT_{gas}} + k_{S,des}\sqrt{p_{end}} V_{LiPb} \quad (5)$$

For desorption tests, the Sieverts' constant can be evaluated as:

$$k_{S,des} = \frac{2}{RT_{gas}} \frac{V_{gas}}{V_{LiPb}} \frac{p_{end}}{\sqrt{p_0} - \sqrt{p_{end}}} \quad (6)$$

Fauvet [18] and Reiter [19, 20] have included an additional contribution, Δp, in the numerator of Equation 6 to account for hydrogen loss from LiPb during the pump-down period. This contribution is not easily determined experimentally because it depends on the properties of the system (pumping speed, recombination and dissociation coefficients of the LiPb, geometry, etc.). To be sure that this term can be neglected, the time to evacuate the chamber must be reduced as much as possible (on the order of seconds): in this case, it is reasonable to assume that the Δp is approximately equal to zero. It should be noticed that both authors did not accurately determine the amount of hydrogen or deuterium dissolved in the various parts of their test section, neither in the loading phase nor in the desorption phase.

5. Numerical calculations in support to the design

In order to support the design, different numerical simulations of the permeation chamber were performed. The aim of these analyses is twofold. On one hand, the thermal behaviour needs to be deepened in order to understand if the operative temperature range is reliable. In particular, the seal between the quartz chamber and the upper flange needs to be kept at a temperature lower than 150 °C, and the instrumentation installed in one the three sleeves can operate at a maximum temperature of 50 °C. On the other hand, it is necessary to quantify the hydrogen distribution in the different domains of the chamber (quartz, tungsten, LiPb, iron, stainless steel) and the time required for the complete solubilisation of the hydrogen contained in the argon/hydrogen gas mixture. To do so, a finite elements method (FEM) 2D axial-symmetric model was developed through the commercial software COMSOL Multiphysics. The CFD model with heat transfer, shown in Chapter 5.1, was used as an input for the tritium transport analysis, in order to have reliable temperature and velocity fields for the general transport equation, as detailed in Chapter 5.2.

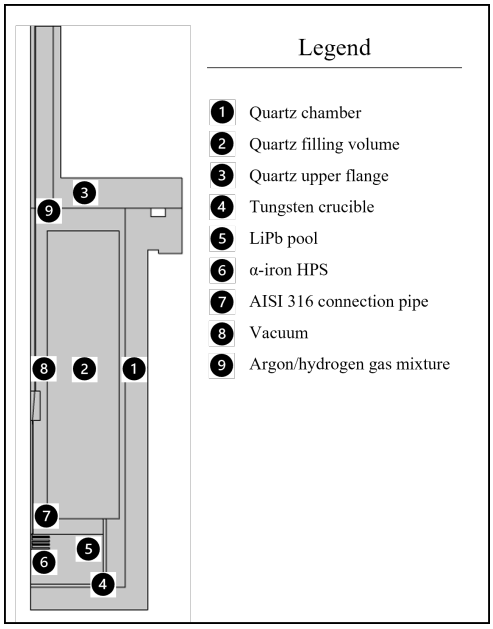

Figure 8: Part of the 2D axial-symmetric geometry for the thermal and transport analyses.

The geometry simulated includes the whole quartz chamber and the assembly up to the gate valve of the sensor line. A schematic drawing of the geometry is displayed in Figure 8 along with the different simulated domains. The AISI 316 connections up to the gate valve are not reproduced in the figure. The geometry was simplified with respect to the actual design adopting a 2D axial-symmetric model, with the aim of reducing the computational effort. In particular:

- Only one sleeve was represented and positioned at the center of the flange.
- The bellow used for the movement of the sensor was considered as a straight pipe.
- The hydrogen permeation sensor was represented with a different geometrical shape, preserving the same surface-to-volume ratio as the one currently mounted in the chamber.

The approach adopted is conservative. In fact, neglecting the other two sleeves reduces the heat removed by external convection with the air; this leads to an overestimation of the temperatures and, hence, of the parasitic solubilisations. For the thermal analysis and the transport analysis, a grid independence of the results was accurately checked by means of the Grid Convergence Index (GCI) method. The Grid Convergence Index method (GCI) is a recommended method [21] evaluated over several hundred computational cases [22]. Three different meshes were used, labeled M1 (finest), M2 (reference mesh) and M3 (coarser). The detailed procedure for the estimation of the GCI can be found in [21]. For the thermal analysis, 8 variables were considered (4 local and 4 global) and reported in Table 5. The average error for the best mesh was calculated as 0.94%. The grid convergence analysis for the transport analysis was conducted considering 11 variables as shown in Table 6 (6 local, 5 global), for which an average GCI equal 1.63% was obtained for the best mesh. For the transport analysis, variables were selected both at the end of the transient and at different times. The finest mesh M1 was adopted for all the calculations.

Table 5: Variables selection for GCI thermal analysis

ID	Variable	Location	Type
1	Max radiosity	AISI 316	Local
2	Max temperature	Chamber	Local
3	Max pressure	Gas	Local
4	Max vorticity magnitude	Sleeve	Local
5	Avg velocity magnitude	Sleeve	Global
6	Avg convective heat flux	Gas	Global
7	Avg velocity magnitude	Sleeve	Global
8	Avg pressure	Gas	Global

Table 6: Variables selection for GCI transport analysis

ID	Variable	Location	Type
1	Max velocity module	Argon	Local
2	Max conc. of H	LiPb	Local
3	Max conc. of H	Tungsten	Local
4	Max conc. of H	Iron	Local
5	Max conc. of H	AISI 316	Local
6	Max conc. of H (diff. time)	LiPb	Local
7	Avg conc. of H	LiPb	Global
8	Avg conc. of H	Tungsten	Global
9	Avg conc. of H_2	Iron	Global
10	Avg conc. of H	AISI 316	Global
11	Avg conc. of H (diff. time)	LiPb	Global

5.1. Thermal analysis

The aim of the thermal analysis is twofold. Firstly, it was necessary to have a precise temperature field and velocity field in order to accurately solve the general transport equation. Secondly, since the maximum operative temperature of the o-ring between the chamber and the upper flange of the test section is 150 °C, it was necessary to verify, in the most severe operative conditions (1000 hPa gas pressure in the chamber at 450 °C), if the seal would have withstanded.

To do so, a thermal analysis was conducted considering the temporal evolution in three reference cases:

1. Permeation chamber in a perfect vacuum condition.
2. Injection of helium at $T = 450$ °C once the steady-state temperature of case 1) was reached.
3. Injection of a mixture of argon+hydrogen (2.99% vol. H_2) at $T = 450$ °C once the steady-state temperature of case 1) was reached.

The first case allows to have an indication of the temperature during operation without gas (i.e. for tightness tests or for degassing procedures). The second case was developed when pressurization tests with pure helium are performed, whereas the last case is representative of real operational conditions. The reference thermophysical properties for lithium-lead were taken from [23] while its radiative emissivity was in accordance with [24]. COMSOL built-in properties of quartz, tungsten, AISI 316, iron, helium and argon were used [25].

Only the temperature field and the velocity field for case 3) are reported for conciseness, Figure 9. It can be observed that the stainless steel connector from the 1/8" pipe of the HPS and the 1/4" pipe is at about 300 °C, whereas the 1/8" pipe has a temperature between 300 and 450 °C, Figure 9a. As it will be seen in Chapter 5.2, this constitutes a possible issue from the viewpoint of permeation and solubilisation. The filling cylinder assumes the role of thermal damper element, reducing the heat load to the upper flange and shielding the flange from the radiative contribution. Due to the buoyancy effect, the velocity

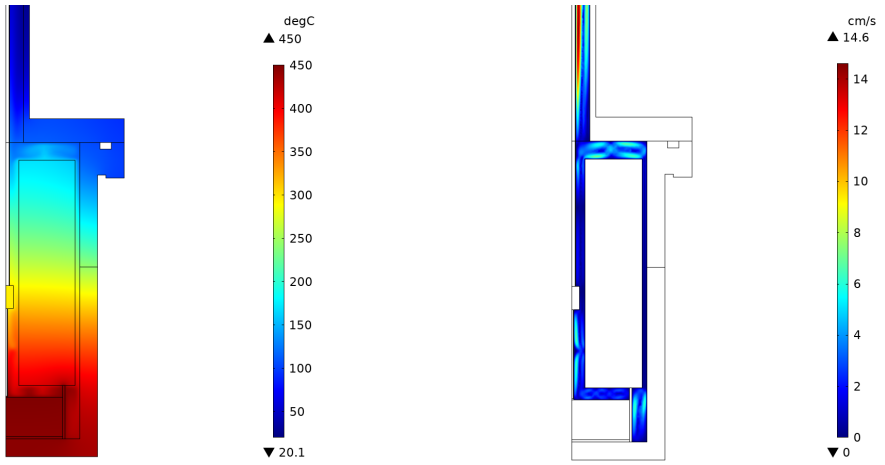

(a) Temperature field [°C] **(b)** Gas velocity field [cm s^{-1}]

Figure 9: Temperature field and velocity field in the 2D axial-symmetric simulation of the permeation chamber.

field (Figure 9b) presents recirculation loops in the zone between the filling cylinder and the upper flange. This effect is enhanced with respect to the case with helium due to the different density of the gases.

As far as the o-ring temperature is concerned, the temperature trend is displayed in Figure 10. The injection of preheated gas at 450 °C (helium or argon) was simulated once the steady-state condition of the temperature for the vacuum case was reached. In case of helium, the temperature in the o-ring results 5 °C higher with respect to the case of argon due to the fact that helium thermal conductivity is about 8 times higher than argon. In both cases, the o-ring temperature is considerably lower than its operational limit (150 °C), with a margin of about 40 °C.

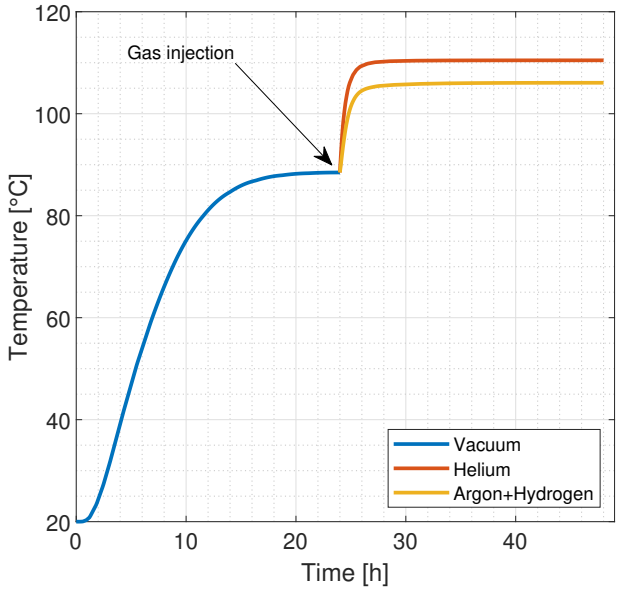

Figure 10: Temperature Trend of the O-Ring cavity

5.2. Transport analysis

A transport analysis was carried out with the aim of analysing the concentration distribution in the different materials of the permeation chamber and estimating the temporal evolution of pressures and concentrations. The model assumes that no leaks are present in the system. The following analysis was performed considering two values of Sieverts' constant: Reiter's correlation [19] and Aiello's correlation [26]. Several values of hydrogen partial pressures injected into the permeation chamber in the range 0.1-100 hPa have been considered. The model solves in the different domains the following passive, scalar, general transport equation:

$$\frac{\partial c}{\partial t} + \vec{u} \cdot \nabla c + \nabla \cdot (-D \nabla c) = 0 \tag{7}$$

where c [mol m^{-3}] is the hydrogen concentration (atomic or molecular) in the i-th domain, $\vec{u}$ [m s^{-1}] is the velocity field, D [m^{-2} s^{-1}] is the diffusion coefficient and $\vec{J} = -D\nabla c + c\vec{u}$ [mol m^{-2} s^{-1}] is the transport flux. Sieverts' law was assumed to apply at the interfaces LiPb/Fe, LiPb/W, LiPb/316 and Fe/316. At each interface, pressure continuity was assumed, leading to the discontinuity of concentrations. For instance, at the interface LiPb/Fe this leads to:

$$\frac{c|_{\partial\Omega_{Fe,LiPb}}}{c|_{\partial\Omega_{LiPb,Fe}}} = K \tag{8}$$

Here, $c|_{\partial\Omega_{Fe,LiPb}}$ is the H concentration of hydrogen evaluated at the Fe/LiPb interface, $c|_{\partial\Omega_{Fe,LiPb}}$ is the concentration at the LiPb/Fe interface and $K = k_{s,Fe}/k_{s,LiPb}$ expresses the ratio between the Sieverts' constant of the sensor membrane with respect to the Sieverts' constant of liquid lithium-lead. Furthermore, the flux continuity must be ensured, i.e.:

$$\vec{J}|_{\partial\Omega_{Fe,LiPb}} = \vec{J}|_{\partial\Omega_{LiPb,Fe}} \tag{9}$$

The hydrogen isotopes permeation through glass materials can be described assuming that Henry's law applies [27]. The pressure continuity at the Argon/Quartz interface can be expressed as:

$$\frac{c|_{\partial\Omega_{Q,Ar}}}{c|_{\partial\Omega_{Ar,Q}}} = k_{h,Q} \cdot RT \tag{10}$$

where $k_{h,Q}$ [mol m^{-3} Pa^{-1}] is the Henry's constant for quartz glass. Henry's constant for quartz glass can be derived from the permeability, expressed as [mol m^{-1} s^{-1} Pa^{-1}]. For the present application, Lee correlation was adopted [28]. More general correlations valid for different types of glasses as a function of the content of glass formers G [mol %], SiO_2+B_2O_3+P_2O_5, can be also adopted, as reported in [27]. The suggested one is Tsugawa correlation [29], which gives 2.29% error for $G = 100\%$ (pure quartz glass) at $T = 450$ °C with respect to Lee.

Finally, the net flow of hydrogen isotopes atoms through a metal and the vacuum or argon or quartz interface could be written as:

$$\vec{J}_H = J_r - J_d \tag{11a}$$

$$\vec{J}_{H_2} = -2J_H \tag{11b}$$

The dissociation flux is given by $J_d = k_d \cdot p$ and the recombination flux by $J_r = k_r \cdot c^2$. Here, k_d [mol m^{-2} s^{-1} Pa^{-1}] is the dissociation constant, k_r [m^4 mol^{-1} s^{-1}] is the recombination constant and p [Pa] is the pressure. In general, the recombination constant, the dissociation constant and the Sieverts' constant are related through the relation $k_d = k_r \cdot k_s^2$ [30]. In Table 7, the main transport properties adopted in this study are reported. It should be observed that the derivation of the recombination constant of LiPb in the case of Aiello was carried out following the approach reported in [31], hence substituting Aiello's correlation in Equation 2 of his paper.

In Figure 11 the temporal evolution of the moles of hydrogen referred to the total amount of hydrogen present in the chamber is shown for a hydrogen partial pressure of 0.1 hPa. The sensor is operated in equilibrium mode. With the adoption of Aiello's correlation, Figure 11a, most of hydrogen is solubilzed into the lithium-lead pool (95%) and the remaining 5% into the other parts. In the quartz, only 0.025% is solubilized. In contrast, in case of Reiter's correlation, Figure 11b, only 17% of hydrogen goes into the LiPb, whereas 71% remains into the argon and about 8% is solubilized into the stainless steel connection pipe. This is due to the fact that the temperature along the axis of the connection pipe varies from 300 °C (in proximity of the stainless steel connector) to 450 °C (in proximity of the welding with the HPS), with a permeability varying in the range $[0.5 - 9.5] \cdot 10^{-12}$ mol m^{-1} s^{-1} Pa$^{-0.5}$. With Aiello's correlation, the permeability at 450 °C is $4.4 \cdot 10^{-11}$ mol m^{-1} s^{-1} Pa$^{-0.5}$, which is from 5 to 88 times higher than AISI 316; with Reiter's correlation it is from 0.2 to 3 times higher, meaning that it is comparable with that of AISI 316. This leads to a higher solubilisation in the steel. To reduce this contribution, an antipermeation coating in Al_2O_3 could be applied at the outer surface of the tube by means of a Pulsed Laser Deposition (PLD) or Atomic Layer Deposition (ALD) [39]. This kind of solution could be taken into account once the experimental measurements of the Sieverts' constant will be carried out.

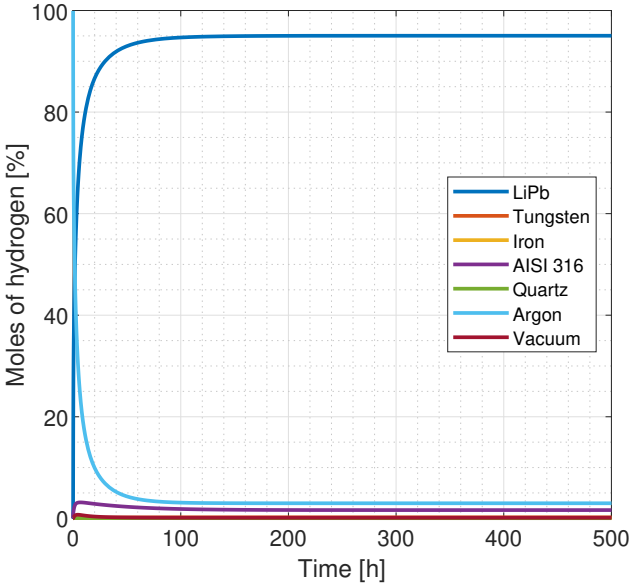

(a) Aiello's correlation.

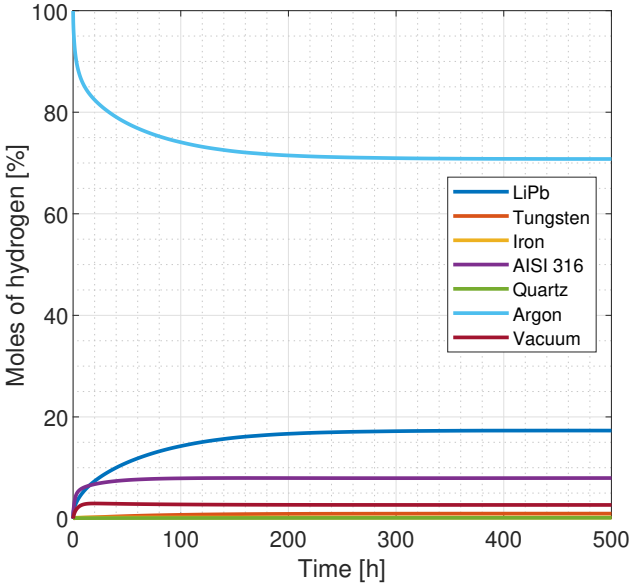

(b) Reiter's correlation.

Figure 11: Temporal evolution of hydrogen solubilisation in the different materials/domains for 0.1 hPa hydrogen pressure in case of (a) Aiello's correlation and (b) Reiter's correlation for Sieverts' constant.

Table 7: Materials properties adopted. Values referred to H isotopologue.

LiPb (15.7 at. % Li)			
Sieverts' constant, Aiello [mol m^{-3} Pa$^{-0.5}$]	$2.37 \cdot 10^{-1} \cdot \exp(-12844/RT)$	Aiello et al.	[26]
Sieverts' constant, Reiter [mol m^{-3} Pa$^{-0.5}$]	$1.31 \cdot 10^{-3} \cdot \exp(-1350/RT)$	Reiter	[19]
Hydrogen diffusivity [m^2 s^{-1}]	$4.03 \cdot 10^{-8} \cdot \exp(-19500/RT)$	Reiter	[19]
Rec. constant, Reiter [m^4 mol^{-1} s^{-1}]	$5.727 \cdot 10^{-2} \cdot \exp(-29717/RT)$	Pisarev et al.	[31]
Rec. constant, Aiello [m^4 mol^{-1} s^{-1}]	$3.141 \cdot 10^{-4} \cdot \exp(-18223/RT)$	Pisarev et al.	[31]
α-iron (bcc)			
Diffusivity [m^2 s^{-1}]	$1.01 \cdot 10^{-7} \cdot \exp(-802.7/T)$	Miller et al.	[32]
Permeability [mol m^{-1} s^{-1} Pa$^{-0.5}$]	$4.10 \cdot 10^{-8} \cdot \exp(-4200/T)$	Gonzalez	[33]
Sieverts' constant [mol m^{-3} Pa$^{-0.5}$]	$4.06 \cdot 10^{-1} \cdot \exp(-3397.3/T)$	(derived value)	
Rec. constant, clean surf. [m^4 mol^{-1} s^{-1}]	$1.61 \cdot 10^{-2} \cdot \exp(2177.2/T)$	Pick&Sonnenberg	[34]
AISI 316			
Diffusivity [m^2 s^{-1}]	$7.30 \cdot 10^{-7} \cdot \exp(-6300/T)$	Grant et al.	[35]
Permeability [mol m^{-1} s^{-1} Pa$^{-0.5}$]	$8.10 \cdot 10^{-7} \cdot \exp(-8190/T)$	Grant et al.	[35]
Sieverts' constant [mol m^{-3} Pa$^{-0.5}$]	$1.11 \cdot \exp(-1890/T)$	(derived value)	
Rec. constant, experimental [m^4 mol^{-1} s^{-1}]	$2.35 \cdot \exp(-70000/RT)$	Waelbroeck et al.	[36]
Tungsten			
Diffusivity [m^2 s^{-1}]	$5.68 \cdot 10^{-10} \cdot \exp(-9300/RT)$	Esteban et al.	[37]
Permeability [mol m^{-1} s^{-1} Pa$^{-0.5}$]	$1.65 \cdot 10^{-11} \cdot \exp(-36200/RT)$	Esteban et al.	[37]
Sieverts' constant [mol m^{-3} Pa$^{-0.5}$]	$2.90 \cdot 10^{-2} \cdot \exp(-26900/RT)$	(derived value)	
Rec. constant, clean surface [m^4 mol^{-1} s^{-1}]	$1.81 \cdot 10^{-1} \cdot T^{-0.5} \cdot \exp(23906/T)$	Ogorodnikova	[38]
Quartz glass			
Diffusivity [m^2 s^{-1}]	$5.65 \cdot 10^{-8} \cdot \exp(-43388/RT)$	Lee et al.	[28]
Permeability [mol m^{-1} s^{-1} Pa^{-1}]	$7.41 \cdot 10^{-14} \cdot \exp(-37154/RT)$	Lee et al.	[28]
Henry's constant [mol m^{-3} Pa^{-1}]	$1.31 \cdot 10^{-6} \cdot \exp(-6234.2/RT)$	(derived value)	

In Figure 12 the time needed to reach 95% of the steady-state condition (i.e., the time needed for the complete solubilisation of hydrogen in the different domains) is reported. The simulations were performed in the range 0.1-100 hPa of partial pressure of hydrogen injected into the chamber. Reiter's correlation predicts higher times for the solubilisation of hydrogen in the LiPb but has a small variation in the range 0.2-10 hPa, corresponding to 7-8 days. Aiello's correlation predicts lower times; in the example at 0.1 hPa, the solubilisation occurs in about 30 hours. For pressures higher than 10 hPa, the time for 95% of solubilisation is 6-7 days. It should be observed that these results are strongly dependent on the value of the diffusion coefficient; for this application, Reiter's diffusion coefficient was adopted [19]. As a future experimental campaign, hydrogen diffusivity in LiPb will be measured taking advantage of the model developed.

Only a fraction of the hydrogen injected into the chamber will be solubilized into the LiPb. In an absorption test, the partial pressure of the hydrogen into the chamber will decrease up to a steady-state value; the value of this pressure will be in equilibrium with the pressure of monoatomic hydrogen in the LiPb, according to Sieverts' law. To have an estimate of the partial pressure in the LiPb, several simulations were performed in the range 0.1-100 hPa, as displayed in Figure 13. With Reiter's correlation, for pressures higher than 2 hPa the partial pressure of monoatomic hydrogen in the LiPb will differ less than 10% with respect to the partial pressure of molecular hydrogen injected. On the other hand, with Aiello the discrepancy is remarkably pronounced. For instance, to have 0.1 hPa in the LiPb, the partial pressure of hydrogen to be injected into the chamber should be 0.7 hPa.

6. Conclusions

Within this paper, the design of a lab-scale facility named HyPer-QuarCh II was presented. The new design takes advantage of the experience gained in previous experimental campaigns and consists in the following:

- New instrumentation, related to high-accuracy pressure transducers, pumping system and new Data Acquisition and Control System (DACS), to perform the tests in the range of pressures representative for both ITER and DEMO reactors;
- New permeation chamber with quartz to metal connections to simplify the conjunction with the other

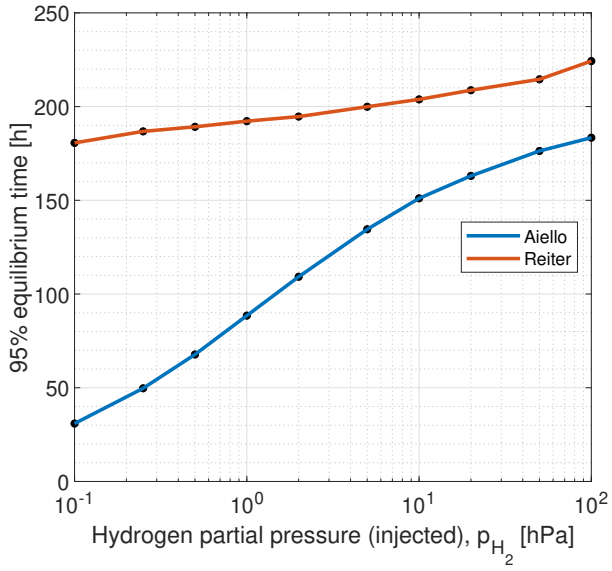

Figure 12: Response time to reach 95% of steady-state of hydrogen solubilisation as a function of the molecular hydrogen in the chamber. Black dots represent a simulation run.

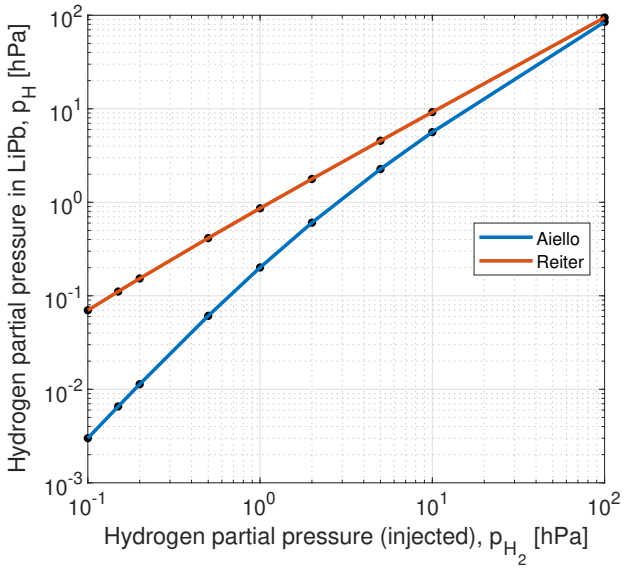

Figure 13: Monoatomic hydrogen partial pressure in liquid LiPb as a function of molecular hydrogen injected into the permeation chamber. Black dots represent a simulation run.

equipment; the sleeves present external groves where O-rings are hosted in order to ensure the coupling between the stainless steel KF connections and the sleeves.

- Reduction of the internal volume of the chamber in order to perform a new measurement of the Sieverts' constant in static LiPb in both absorption and desorption mode.

As a support to the design, a computation model was developed through COMSOL Multiphysics in order to study the thermal behaviour and the hydrogen transport in the permeation chamber. The results showed that the in the most severe operational conditions (i.e., 450 °C and 1000 hPa injected gas) the sealing between the chamber and the upper flange is preserved, with a margin of about 40 °C on the working limit. From the transport analysis, it was shown that if Aiello's correlation holds, most of hydrogen will be solubilized in the LiPb, whereas small amount will be solubilized in the other materials. However, with Reiter's correlation, the stainless steel connection of the HPS could represent a sink for hydrogen, and a permeation reduction coating should be applied. A test duration for a pressure higher than 10 hPa was foreseen to last about one week according to Reiter's diffusivity. Moreover, a correlation between the partial pressure of hydrogen injected into the chamber and the partial pressure of monoatomic hydrogen into the LiPb was found.

It should be noted that the facility shown in this article has just been built; the on-going experimental campaign is scheduled for completion in the first part of 2022.

Acknowledgments

This work has been carried out within the framework of the EUROfusion Consortium and has received funding from the Euratom research and training programme 2014-2018 and 2019-2020 under grant agreement No 633053. The views and opinions expressed herein do not necessarily reflect those of the European Commission.

References

[1] J. Aubert, G. Aiello, D. Alonso, T. Batal, R. Boullon, S. Burles, B. Cantone, F. Cismondi, A. Del Nevo, L. Maqueda, A. Morin, E. Rodríguez, F. Rueda, M. Soldaini, J. Vallory, Design and preliminary analyses of the new Water Cooled Lithium Lead TBM for ITER, Fusion Engineering and Design 160 (2020) 111921. doi:https://doi.org/10.1016/j.fusengdes.2020.111921.

[2] A. Del Nevo, P. Arena, G. Caruso, P. Chiovaro, P. Di Maio, M. Eboli, F. Edemetti, N. Forgione, R. Forte, A. Froio, F. Giannetti, G. Di Gironimo, K. Jiang, S. Liu, F. Moro, R. Mozzillo, L. Savoldi, A. Tarallo, M. Tarantino, A. Tassone, M. Utili, R. Villari, R. Zanino, E. Martelli, Recent progress in developing a feasible and integrated conceptual design of the WCLL BB in EUROfusion project, Fusion Engineering and Design 146 (2019) 1805–1809. doi:https://doi.org/10.1016/j.fusengdes.2019.03.040.

[3] G. Federici, L. Boccaccini, F. Cismondi, M. Gasparotto, Y. Poitevin, I. Ricapito, An overview of the EU breeding blanket design strategy as an integral part of the DEMO design effort, Fusion Engineering and Design 141 (2019) 30–42. doi:https://doi.org/10.1016/j.fusengdes.2019.01.141.

[4] F. Cismondi, et al., Progress of the conceptual design of the European DEMO breeding blanket, tritium extraction and coolant purification systems, Fusion Engineering and Design 157 (2020) 111640. doi:https://doi.org/10.1016/j.fusengdes.2020.111640.

[5] P. Fichet, A. Bultel, S. Markelij, C. Moreno, Review of the different techniques to analyse tritium, Tech. Rep. TRANSAT WP02-D2.1, CEA, France, https://transat-h2020.eu/wp-content/uploads/2020/04/TRANSAT_D2_1.pdf (7 2018).

[6] A. Ciampichetti, M. Zucchetti, I. Ricapito, M. Utili, A. Aiello, G. Benamati, Performance of a hydrogen sensor in Pb–16Li, Journal of Nuclear Materials 367-370 (2007) 1090–1095. doi:https://doi.org/10.1016/j.jnucmat.2007.03.250.

[7] I. Nicolotti, M. Utili, L. Candido, M. Zucchetti, A hydrogen sensor for liquid-metal breeding blankets, Transactions of the American Nuclear Society 112 (2015) 193–196, 2015 ANS Annual Meeting, San Antonio, TX.

[8] L. Candido, I. Nicolotti, M. Utili, M. Zucchetti, Design optimization of a hydrogen sensor for ITER Pb16Li blankets, IEEE Transactions on Plasma Science 45 (7) (2017) 1831–1836. doi:10.1109/TPS.2017.2710218.

[9] I. Ricapito, A. Aiello, A. Bükki-Deme, J. Galabert, C. Moreno, Y. Poitevin, D. Radloff, A. Rueda, A. Tincani, M. Utili, Tritium technologies and transport modelling: main outcomes from the European TBM project, Fusion Engineering and Design 136 (2018) 128–134. doi:https://doi.org/10.1016/j.fusengdes.2018.01.023.

[10] M. Utili, A. Ciampichetti, A. Aiello, I. Ricapito, P. Agostini, F. Desideri, K. Liger, Design of a multipurpose laboratory scale apparatus for the investigation of hydrogen isotopes in pbli and permeation technologies, Fusion Engineering and Design 87 (7) (2012) 1342–1346.

[11] L. Candido, M. Cantore, E. Galli, R. Testoni, M. Zucchetti, M. Utili, A. Ciampichetti, Characterization of Pb-15.7Li hydrogen isotopes permeation sensors and upgrade of HyPer-Quarch experimental device, IEEE Transactions on Plasma Science 48 (6) (2020) 1505–1511. doi:10.1109/TPS.2020.2974937.

[12] L. Candido, M. Utili, M. Zucchetti, A. Ciampichetti, P. Calderoni, Development of advanced hydrogen permeation sensors to measure Q2 concentration in lead-lithium eutectic alloy, Fusion Engineering and Design 124 (2017) 735–739. doi:https://doi.org/10.1016/j.fusengdes.2017.05.012.

[13] K. Korsah, R. A. Kisner, C. L. Britton, P. Ramuhalli, D. W. Wootan, N. C. Anheier, A. A. Diaz, E. H. Hirt, R. B. Vilim, H. T. Chien, et al., Sensor technology assessment for advanced reactors, Tech. Rep. ORNL/TM-2016/337 R1, Oak Ridge National Laboratory (2017). doi:10.2172/1345781.

[14] L. Candido, M. Cantore, E. Galli, R. Testoni, M. Zucchetti, M. Utili, A. Ciampichetti, Characterization of pb-15.7li hydrogen isotopes permeation sensors and upgrade of hyper- quarch experimental device, IEEE Transactions on Plasma Science 48 (6) (2020) 1505–1511. doi:https://doi.org/10.1109/TPS.2020.2974937.

[15] M. R. Shulz, K. Nagatou, A. von der Weth, F. Arbeiter, V. Pasler, Analytical solution of a gas release problem considering permeation with time-dependent boundary conditions, Journal of Computational and Theoretical Transport 49 (7) (2020) 389–412. doi:https://doi.org/10.1080/23324309.2020.1828469.

[16] P. W. Humrickhouse, Permeation of multiple isotopes in the transition between surface and diffusion-limited regimes, Tritium Focus Group meeting (Idaho National Laboratory, 2014).

[17] C. Alberghi, L. Candido, D. Martelli, F. Papa, M. Utili, M. Zucchetti, Study on hydrogen isotopes permeators adopting secondary surfaces, Preprint submitted to Journal of Membran Science (2021).

[18] P. Fauvet, J. Sannier, Hydrogen behaviour in liquid 17Li83Pb alloy, Journal of Nuclear Materials 155-157 (PART 1) (1988) 516–519.

[19] F. Reiter, Solubility and diffusivity of hydrogen isotopes in liquid pb-17li, Fusion Engineering and Design 14 (3) (1991) 207–211. doi:doi.org/10.1016/0920-3796(91)90003-9.

[20] F. Reiter, J. Camposilvan, G. Gervasini, R. Rota, Interaction of hydrogen isotopes with the liquid eutectic alloy 17Li83Pb, ECSC, EEC, EAEC Luxembourg., 1986.

[21] P. Roache, K. Ghia, F. White, Editorial policy statement on the control of numerical accuracy, Journal of Fluids Engineering 108 (1), 078001 (1986). doi:https://doi.org/10.1115/1.2960953.

[22] M. Casey, T. Wintergerste, Industrial Computational Fluid Dynamics of Single-Phase Flows, 1st Edition, ERCOFTAC Best Practice Guidelines, 1975.

[23] D. Martelli, A. Venturini, M. Utili, Literature review of lead-lithium thermophysical properties, Fusion Engineering and Design 138 (2019) 183–195. doi:https://doi.org/10.1016/j.fusengdes.2018.11.028.

[24] F. Okino, S. Konishi, Emissivity measurement of pbli droplets in a vacuum for heat recovery by radiation, Fusion Engineering and Design 160 (2020) 111961. doi:https://doi.org/10.1016/j.fusengdes.2020.111961.

[25] COMSOL Multiphhysics, v. 5.6, http://www.comsol.com/, Accessed: 2021-01-31.

[26] A. Aiello, A. Ciampichetti, G. Benamati, Determination of hydrogen solubility in lead lithium using sole device, Fusion Engineering and Design 81 (1) (2006) 639–644. doi:doi.org/10.1016/j.fusengdes.2005.06.364.

[27] T. Welter, R. Müller, J. Deubener, U. Marzok, S. Reinsch, Hydrogen permeation through glass, Frontiers in Materials 6 (2020) 342. doi:https://doi.org/10.3389/fmats.2019.00342.

[28] R. W. Lee, R. C. Frank, D. E. Swets, Diffusion of hydrogen and deuterium in fused quartz, The Journal of Chemical Physics 36 (4) (1962) 1062–1071. doi:https://doi.org/10.1063/1.1732632.

[29] R. T. Tsugawa, I. Moen, P. E. Roberts, P. C. Souers, Permeation of helium and hydrogen from glass-microsphere laser targets, Journal of Applied Physics 47 (5) (1976) 1987–1993. doi:https://doi.org/10.1063/1.322924.

[30] I. Ali-Khan, K. Dietz, F. Waelbroeck, P. Wienhold, The rate of hydrogen release out of clean metallic surfaces, Journal of Nuclear Materials 76-77 (1978) 337–343. doi:https://doi.org/10.1016/0022-3115(78)90167-8.

[31] A. Pisarev, T. Tanabe, T. Terai, G. Benamati, M. Mullin, Modeling of in-pile experiments on tritium release from molten lithium-lead, Journal of Nuclear Science and Technology 39 (4) (2002) 377–381. doi:https://doi.org/10.1080/18811248.2002.9715207.

[32] R. F. Miller, J. B. Hudson, G. S. Ansell, Permeation of hydrogen through alpha iron, Metallurgical Transactions A 6 (1) (1975) 117–121.

[33] O. D. Gonzalez, Permeation of hydrogen and deuterium in alpha-iron, Transactions of the Metallurgical Society of AIME 239 (1969) 929–930.

[34] M. Pick, K. Sonnenberg, A model for atomic hydrogen-metal interactions — application to recycling, recombination and permeation, Journal of Nuclear Materials 131 (2) (1985) 208–220. doi:https://doi.org/10.1016/0022-3115(85)90459-3.

[35] D. Grant, D. Cummings, D. Blackburn, Hydrogen in 316 steel — diffusion, permeation and surface reaction, Journal of Nuclear Materials 152 (2) (1988) 139–145. doi:https://doi.org/10.1016/0022-3115(88)90319-4.

[36] F. Waelbroeck, J. Winter, P. Wienhold, Influence of the wall temperature on hydrogen recycling phenomena in an ss simulation apparatus, Journal of Nuclear Materials 103 (1981) 471–475. doi:https://doi.org/10.1016/0022-3115(82)90642-0.

[37] G. Esteban, A. Perujo, L. Sedano, K. Douglas, Hydrogen isotope diffusive transport parameters in pure polycrystalline tungsten, Journal of Nuclear Materials 295 (1) (2001) 49–56. doi:https://doi.org/10.1016/S0022-3115(01)00486-X.

[38] O. Ogorodnikova, Recombination coefficient of hydrogen on tungsten surface, Journal of Nuclear Materials 522 (2019) 74–79. doi:https://doi.org/10.1016/j.jnucmat.2019.05.017.

[39] M. Utili, S. Bassini, S. Cataldo, F. Di Fonzo, M. Kordac, T. Hernandez, K. Kunzova, J. Lorenz, D. Martelli, B. Padino, A. Moroño, M. Tarantino, C. Schroer, G. A. Spagnuolo, L. Vala, M. Vanazzi, A. Venturini, Development of anti-permeation and corrosion barrier coatings for the wcll breeding blanket of the european demo, Fusion Engineering and Design 170 (2021) 112453. doi:https://doi.org/10.1016/j.fusengdes.2021.112453.